



Photocarrier transport of ferroelectric photovoltaic thin films detected by the magnetic dynamics of adjacent ferromagnetic layers

Yujun Zhang ^{1,2,*}, Ji Ma^{3,4,*}, Keisuke Ikeda⁵, Yasuyuki Hirata⁵, Kohei Yamagami⁵, Christian Schüßler-Langeheine ⁶, Niko Pontius⁶, Haojie Han⁴, Yuanhua Lin⁴, Cewen Nan⁴, and Hiroki Wadati^{2,7}

¹*Institute of High Energy Physics, Chinese Academy of Sciences, Yuquan Road 19B, Shijingshan District, Beijing 100049, China*

²*Department of Material Science, Graduate School of Science, University of Hyogo, Ako, Hyogo 678-1297, Japan*

³*Kunming University of Science and Technology, Kunming, Yunnan 650093, China*

⁴*State Key Lab of New Ceramics and Fine Processing, School of Materials Science and Engineering, Tsinghua University, Beijing 100084, China*

⁵*Institute for Solid State Physics, University of Tokyo, 5-1-5 Kashiwanoha, Chiba 277-8581, Japan*

⁶*Helmholtz-Zentrum Berlin für Materialien und Energie GmbH, Albert-Einstein-Straße 15, D-12489 Berlin, Germany*

⁷*Institute of Laser Engineering, Osaka University, Suita, Osaka 565-0871, Japan*



(Received 7 February 2023; revised 28 April 2023; accepted 1 June 2023; published 21 June 2023)

We have observed photocarrier transport behaviors in BiFeO₃/La_{1-x}Sr_xMnO₃ (BFO/LSMO) heterostructures by using time-resolved synchrotron x-ray magnetic circular dichroism in reflectivity. The magnetization of LSMO layers was used as a probe of photo-induced carrier dynamics in the photovoltaic BFO layers. During the photo-induced demagnetization process, the decay time of LSMO ($x=0.2$) magnetization strongly depends on the ferroelectric polarization direction of the BFO layer. The variation of decay time should be attributed to the different sign of accumulated photocarriers at the BFO/LSMO interface induced by the photovoltaic effect of the BFO layer. The photocarriers can reach the BFO/LSMO interface and influence the magnetization distribution in the LSMO layers within the timescale of ~ 100 ps. Our results provide a novel strategy to investigate carrier dynamics and mechanisms of optical control of magnetization in thin film heterostructures.

DOI: [10.1103/PhysRevB.107.L220303](https://doi.org/10.1103/PhysRevB.107.L220303)

I. INTRODUCTION

Ferroelectric photovoltaic (FEPV) effect [1–4] has attracted a great amount of research attention due to its unique advantages of over-bandgap photovoltage and switchable photocurrent, compared to the conventional photovoltaic effect in p-n junction-based solar cells. On one hand, FEPV materials can generate photovoltage larger than their bandgaps, which is especially helpful for application of narrow-bandgap FEPV materials [5,6]. On the other hand, ferroelectric (FE) materials exhibit switchable electric polarization, which can couple with the direction of the photocurrent, adding much flexibility for manipulation of FEPV effects in photovoltaic devices [7–10].

Meanwhile, multiferroic heterostructures exhibiting both ferroelectricity and ferromagnetism [11–14] have been intensely investigated for a few decades, aiming at both interfacial magnetoelectric coupling mechanisms [15,16] and potential applications such as memory devices [17,18], sensors [19], etc. Generally, the manipulation of magnetism in multiferroic heterostructures can be realized by the strain, interfacial charge accumulation, and interfacial exchange coupling accompanied with the switching of the electric polarization. Light excitation can act as an additional route

to control the magnetism and transport properties in multiferroic heterostructures when the FE layer exhibits FEPV effect. It has been reported that generation and transport of photocarriers into the ferromagnetic (FM) layers can modify their magnetism and electric transport behaviors [20–22]. Nevertheless, the dynamic process of the carrier transport is rarely investigated in multiferroic heterostructures with FEPV effect.

BiFeO₃ (BFO) [5–10,23] is one of the most intensely studied FEPV materials with outstanding FEPV properties. Previous works about photo-induced dynamics in BFO mainly focus on the transient lattice change in ps to ns timescales induced by ultrafast optical illumination [24–26]. Daranciang *et al.* [27] reported ultrafast FEPV response in BFO also from the view of transient lattice change. More direct observation of photocarrier transport dynamics induced by FEPV effect of BFO is still absent. Here we select BFO/(La,Sr)MnO₃ (LSMO) multiferroic heterostructure as a model system to investigate the effects of photocarrier transport upon the magnetism of the LSMO layer in the time domain. Photocarrier transport dynamics is detected by element-specific time-resolved x-ray magnetic circular dichroism in reflectivity (XMCDR) [28,29]. Finite penetration of XMCDR provides sensitivity to the depth profile of magnetization, and element specificity of XMCDR ensures that the magnetic signal comes from the LSMO layer. The photo-induced magnetic dynamics of LSMO layer strongly depend on the direction of the FE polarization of the BFO layer, as well as the Sr concentration

*These authors contributed equally to this work.

†zhangyujun@ihp.ac.cn

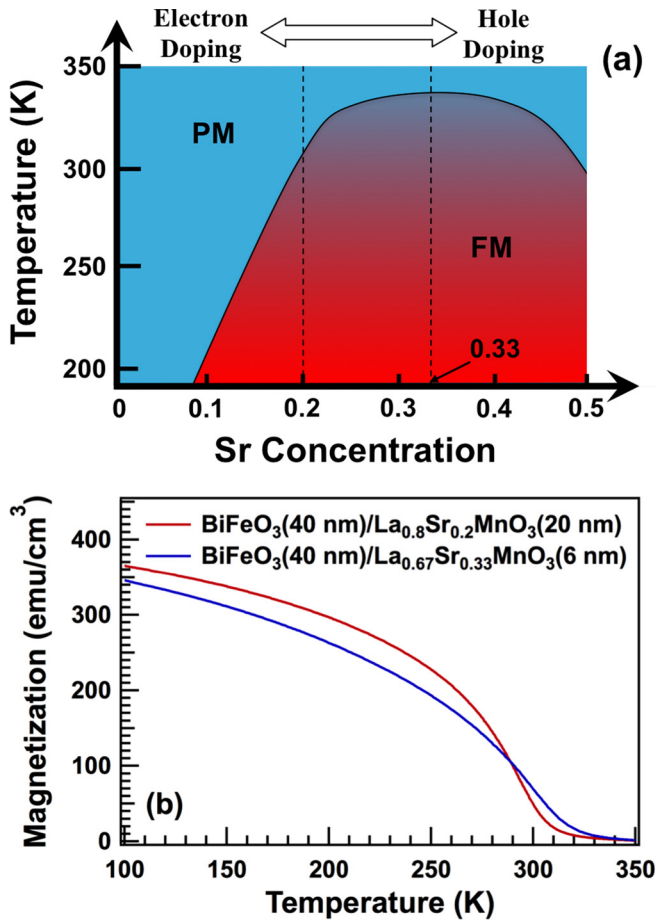


FIG. 1. (a) Schematic phase diagram of LSMO. (b) $M - T$ curves of the BFO/LSMO multiferroic heterostructures.

in the LSMO layer, which can be explained by transient carrier accumulation at the multiferroic interface.

II. METHODS AND BASIC SAMPLE CHARACTERIZATIONS

Epitaxial BFO/La_{1-x}Sr_xMnO₃ (LSMO_x, $x = 0.2$ and 0.33) thin film heterostructures and SrTiO₃ (STO)/LSMO_x ($x = 0.2$ and 0.33) reference samples were fabricated by pulsed laser deposition. LSMO_x and BFO (or STO) layers were grown in sequence on STO(001) single-crystalline substrates. The nominal thickness of the BFO, STO, LSMO_{0.2}, and LSMO_{0.33} layers are 40, 40, 20, and 6 nm, respectively. The detailed growth parameters were reported elsewhere [20]. The epitaxial growth of the films could be confirmed by x-ray diffraction $\theta - 2\theta$ scans (measured by Panalytical Empyrean and Rigaku D x-ray diffractometers with Cu K_{α} radiation), as shown in Fig. S1.

As schematically shown in Fig. 1(a), the paramagnetic (PM)-FM transition temperature (T_C) of LSMO depends on the Sr concentration [30,31]. Although the T_C of LSMO should depend on not only composition but also thickness, LSMO_{0.2} still exhibits slightly lower T_C than that of LSMO_{0.33}, as confirmed by the magnetization-temperature ($M - T$) curves in Fig. 1(b). The magnetometry

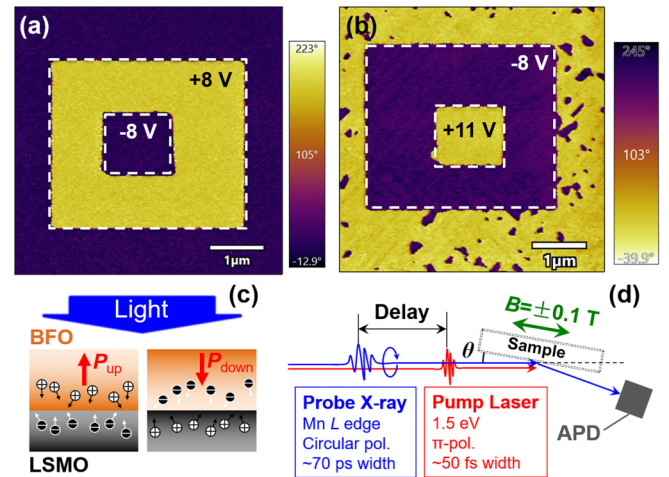


FIG. 2. Out-of-plane PFM images of the BFO/LSMO multiferroic heterostructures with (a) “up” and (b) “down” FE polarization. The regions enclosed by dashed line were scanned by applying tip bias before the PFM measurements. The value of tip bias is indicated in the corresponding region. The color bars show the PFM phase. (c) Schematic of the FEPV-effect-induced carrier transport in BFO/LSMO heterostructures. The deeper and lighter colors indicate the accumulation of positive and negative charge, respectively. (d) Setup of the time-resolved XMCD experiment.

measurements were conducted by a superconducting quantum interference device (SQUID, Quantum Design).

The pristine out-of-plane polarization of the BFO layers is pointing out of the film surface (defined as polarization “up”, P_{up}), as confirmed by the piezoelectric force microscopy (PFM) results shown in Fig. 2(a). The out-of-plane polarization of BFO can be switched to “down” [P_{down} , pointing into the film surface, Fig. 2(b)] by applying DC voltage in water [20,32]. The PFM experiments were performed in ambient conditions at room temperature with an atomic force microscopy system (Infinity, Asylum Research). The STO-capped samples act as zero-polarization references to compare with the BFO/LSMO samples.

Optical excitation above the bandgap of BFO (~ 2.8 eV [33]) is expected to generate free photocarriers. The internal electric field of FE polarization can separate the photocarriers and drive electrons and holes to opposite directions. The photocarriers transported to the BFO/LSMO interface can break the local electric balance, leading to the modulation of carrier density in the LSMO layer, as schematically shown in Fig. 2(c).

Here we design pump-probe experiments to investigate the dynamic modulation of LSMO magnetism by the pump laser. The time-resolved XMCD measurements were carried out at beamline UE56/1-ZPM (FEMTOSPEX) of BESSY II by using the setup shown in Fig. 2(d). X ray with fixed circular polarization at the Mn L edge was used and an in-plane magnetic field of ± 0.1 T was switched to observe the magnetic contrast in reflectivity. The reflectivity was detected with an avalanche photodiode (APD) and boxcar integrated. A Ti:sapphire laser (frequency doubled, $\lambda = 400$ nm, $h\nu \sim 3$ eV, π polarization, 3 kHz, pulse width ~ 50 fs) was employed as the pump source. For the measurement of the LSMO_{0.2} sample,

the full width at half maximum (FWHM) spot sizes (horizontal \times vertical) of the pump laser and the probe x ray were around 0.19×0.14 mm² and 0.12×0.12 mm², respectively. For the measurement of LSMO_{0.33} sample, the FWHM spot sizes (horizontal \times vertical) of the pump laser and the probe x ray were around 0.22×0.28 mm² and 0.11×0.12 mm², respectively. The time resolution of the measurements was limited to ~ 70 ps by the pulse width of the probe x ray. The pumped and unpumped signals were collected alternatively by recording the contributions from the pumped and unpumped bunches. The samples were cooled down to 200 K by a liquid N₂ flow cryostat. The measurements of LSMO_{0.2} and LSMO_{0.33} samples were conducted with pump fluence of 20 and 11.65 mJ/cm², respectively. The laser fluences are calibrated fluences which are absorbed by the samples.

According to the reported optical properties of BFO [34–36] and STO [37–39], 40 nm of BFO can absorb most ($\sim 95\%$) of the 400-nm pump laser, while STO, whose bandgap is ~ 3.7 eV, can only absorb $<10\%$ of the 400-nm pump laser, when taking the incident angle of $\theta = 15^\circ$ into consideration. Most of the pump fluence was absorbed by the BFO layer in BFO/LSMO samples, while for STO/LSMO reference samples, the LSMO is nearly directly pumped by the 400-nm laser. Thus, the magnetic dynamics of BFO/LSMO samples observed in our setup mainly reflects the effects induced by optical pumping of the BFO layer. The penetration depth of the x ray at the Mn *L* edges is comparable for BFO and STO (estimated by CXRO [40]), thus the probing depth of XMCDR is similar for all the samples.

The calculation of XMCDR was conducted by the REMAGX software [41]. The nonresonant optical constants (real and imaginary parts of the refractive index, δ and β) of BFO, STO, and LSMO were obtained from the optical database of Henke [40,42]. For LSMO layers, the imaginary part of the refractive index β as well as its magnetic dichroism β_M at the Mn *L* edge were extracted from Ref. [43] (ignoring the Sr-concentration dependence of the spectral shape) and scaled to fit into the optical constant data from the Henke's database. Consequently, Kramers-Kronig transformation was conducted on the imaginary parts to obtain the real parts of the optical constants (including the magnetic real part δ_M). For all the calculations, the roughness of all the layers were set as zero, and the angular and energy resolution was set as 5 mrad and 1 eV, respectively.

III. RESULTS AND DISCUSSIONS

XMCDR at the Mn *L* edges contains information about the Mn magnetization near the BFO/LSMO interface. The static reflectivity and XMCDR of the LSMO_{0.2} samples with P_{up} and P_{down} , as well as the STO-capped sample, are shown in Fig. S2. Oscillations of the specular reflectivity [Figs. S2(a)–S2(c)] indicate perfect surface and interface quality of the heterostructures. XMCDR also exhibits oscillations and an incident angle of $\theta = 15^\circ$ was chosen for the following time-resolved measurements to obtain the best magnetic contrast. Energy scans at the Mn *L* edges show significant circular dichroism of the reflectivity signal [Figs. S2(d)–S2(f)]. The time-resolved measurements were conducted at optimized

photon energies with large XMCDR for each sample. The magnetic hysteresis of the reflectivity signal shown in Fig. S3 confirms the FM nature of the LSMO layer. The LSMO_{0.33} samples show similar properties as that of the LSMO_{0.2} samples.

Light excitation can cause demagnetization of the LSMO layers. There are several possible contributions of the demagnetization. One is photo-induced demagnetization by the pump laser transmitted through the BFO layer. Second is the heat diffusion from the BFO layer, which is heated by absorbing the main part of the pump fluence. These two contributions should happen in the time scale of tens to hundreds of ps (see Ref. [44] and Supplemental Material [45]). Meanwhile, according to the schematic magnetic phase diagram of LSMO shown in Fig. 1(a), the PM-FM transition temperature of LSMO strongly depends on the Sr doping concentration at $x \sim 0.2$ and exhibits weak dependence on the Sr concentration at $x \sim 0.33$. Thus it is expected that the magnetic dynamics of LSMO_{0.2} samples will be significantly influenced by the out-of-plane polarization direction of the BFO layer, whereas that of the LSMO_{0.33} samples will be barely influenced by the FEPV effect of the BFO layer. These expectations were confirmed by the time-resolved XMCDR measurements depicted in Fig. 3. The delay scans are fitted by the function,

$$I(t) = I_0 - I_1 \exp(-t/\tau_{\text{decay}})H(t), \quad (1)$$

convolved with a 70-ps-wide Gaussian time-resolution function. $H(t)$ is the Heaviside step function and the parameter τ_{decay} is used for evaluation of the demagnetization timescale.

For the LSMO_{0.2} samples, “up” polarization of the BFO obviously induced a faster demagnetization of the LSMO layer, while the “down” polarization did the opposite effect. The τ_{decay} of P_{up} , P_{down} , and STO-capped samples are determined as 39.9 ± 0.2 , 122.3 ± 6.8 , and 82.3 ± 1.5 ps, respectively. While for the LSMO_{0.33} samples, the τ_{decay} of P_{up} , P_{down} , and STO-capped samples are determined as 70.3 ± 0.3 , 70.0 ± 0.3 , and 69.6 ± 0.2 ps, respectively, indicating the negligible role of BFO polarization on the magnetic dynamics of Mn magnetization in LSMO_{0.33} samples. STO capping layers barely absorb the 400-nm pump laser, hence the magnetic dynamics of the STO-capped samples can be regarded as a LSMO single layer reference. The distinct magnetic dynamics of LSMO_{0.2} samples with different BFO polarization should be attributed to the fact that the PM-FM phase transition temperature changes steeply with the Sr concentration for LSMO_{0.2} [left dashed line in Fig. 1(a)], and electron/hole doping has the opposite effect on the magnetization. Different charge signs of the photocarriers will effectively lead to transient changes of the T_C of LSMO, compensating or accelerating the demagnetization process. While the PM-FM phase transition temperature of LSMO_{0.33} is near the maximum [right dashed line in Fig. 1(a)] when changing the Sr concentration. Either electron or hole doping will induce similar decrease of magnetization in LSMO_{0.33} samples.

Due to the difference of the angle and energy profile of the reflectivity, the absolute value of the pump effect can vary. Thus in Fig. 3 we normalized the maximum pump effect to the same value for comparison. We have confirmed by theoretical calculation that the dynamic behaviors of

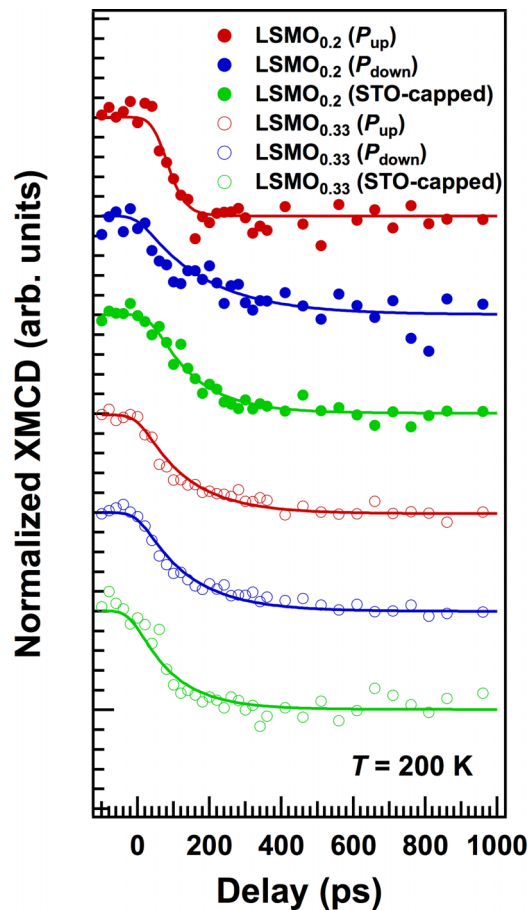


FIG. 3. Magnetic dynamics of the heterostructure samples. The solid lines show the fitting results by using the function (1). Pump effects of all the samples are normalized to 1 by scaling the $I_0=I_1=1$ and the data are vertically shifted. The incident angle was kept at $\theta = 15^\circ$ and the photon energy varied for different samples and was chosen to maximize the XMCDR signal.

XMCDR should hardly depend on the reflection angle or photon energy, as depicted in Fig. 4. Assuming the static magnetization of $\text{LSMO}_{0.2}$ as M , by varying the size of magnetization from $0M$ to $1.5M$ (by scaling the energy-dependent β_M) in the $\text{BFO}(40 \text{ nm})/\text{LSMO}_{0.2}(20 \text{ nm})$ sample, the angular and energy dependence of the XMCDR exhibit similar shape [Figs. 4(a) and 4(b), left axes] and different size. Figure 4(c) shows the roughly linear dependence of calculated XMCDR upon the size of magnetization at various energy and reflection angle. By conducting linear fit of calculated XMCDR against the magnetization at different energy and reflection angle in Figs. 4(a) and 4(b), the R-square values of the fitting is plotted on the right axes of Figs. 4(a) and 4(b). It could be noticed that the linear relationship between XMCDR and the magnetization only breaks down at reflection angles when the XMCDR is close to zero. Thus, when choosing the energy and reflection angle at a local maximum of the XMCDR, such as cases shown in Fig. S2, the linear relationship between XMCDR and M is well preserved. Consequently, the transient XMCDR should only be proportional to the magnetization of LSMO and independent on the reflection angle and photon energy. Note that the calculated angle/energy dependence of

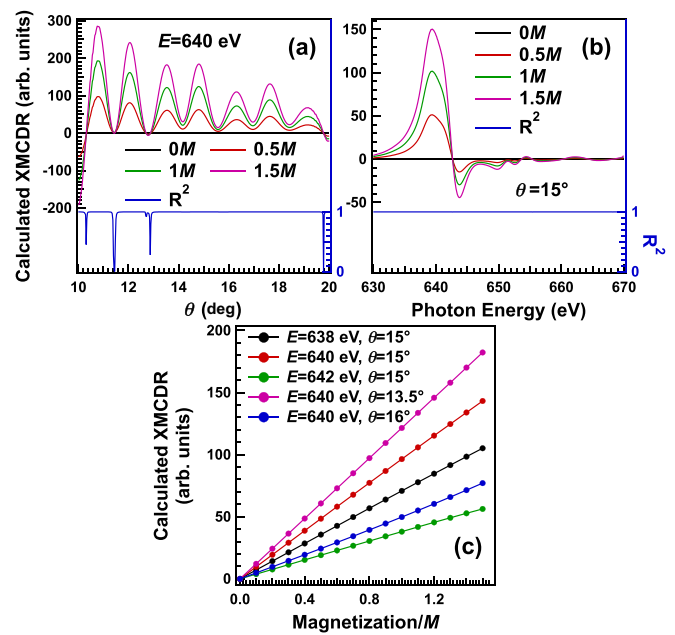


FIG. 4. Calculated (a) angle and (b) energy dependence of XMCDR with different size of magnetization in the $\text{LSMO}_{0.2}$ layer of the $\text{BFO}(40 \text{ nm})/\text{LSMO}_{0.2}(20 \text{ nm})/\text{STO}$ heterostructure. The left axes show the calculated XMCDR and the right axes show the R-square value obtained from linear fitting of calculated XMCDR against the magnetization. (c) Dependence of calculated XMCDR against the LSMO magnetization (in the unit of static magnetization of $\text{LSMO}_{0.2}$, M) at selected energy and reflection angle.

XMCDR differs from the real experimental data, because the angle/energy dependence of resonant reflectivity and XMCDR is very sensitive to the thickness/roughness of distinct layers. Note that choosing the reflection angle at a local maximum of the XMCDR could also minimize the contribution of the thermal expansion of the BFO layer, as discussed in detail in Supplemental Material and Fig. S4 [45].

According to the modification of magnetic dynamics induced by the BFO polarization, the detailed photocarrier transport behavior can be clarified. The photocarrier induced by 400-nm light illumination can be transported to the BFO/LSMO interface by FEPV effect. For the P_{up} samples, the positive charge will move towards the interface, while for the P_{down} samples, the negative charge will move towards the interface. There are two possible regimes of the carrier transport at the BFO/LSMO interface. The photocarriers can either move across the interface and be injected into the LSMO layers, or accumulate at the interface, depending on the interfacial potential barrier.

In case of the injection regime, due to the insulating nature of the STO substrate, P_{up} will induce hole doping in the $\text{LSMO}_{0.2}$ layer, resulting in increase of magnetization, while P_{down} injects electrons into the $\text{LSMO}_{0.2}$ layer, leading to decrease of its magnetization. This contradicts with the experimental observations in Fig. 4, where P_{up} accelerates the demagnetization and P_{down} slows down the demagnetization, with respect to the STO-capped sample.

Thus, the accumulation regime should be considered to explain the magnetic dynamics shown in Fig. 3. When the

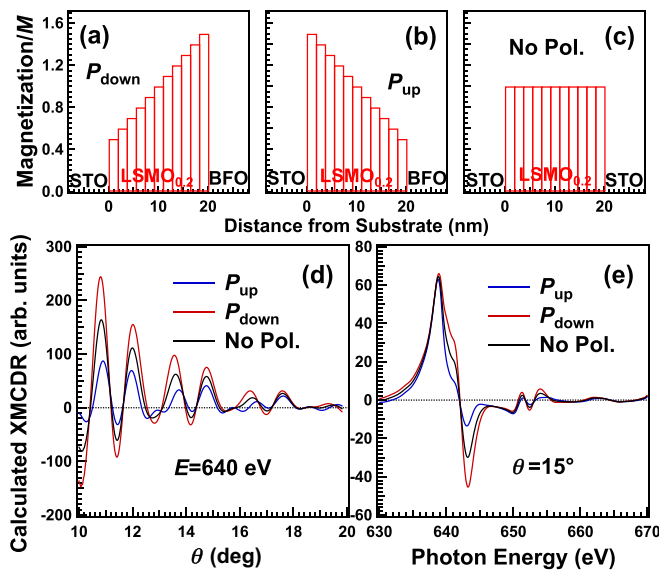


FIG. 5. (a)–(c) Supposed transient magnetization profiles of the $\text{LSMO}_{0.2}$ layer caused by FEPV-induced charge redistribution. Calculated (d) angle and (e) energy dependence of the transient XMCDR using the supposed magnetic profiles.

photocarriers in the BFO layer accumulate at the BFO/LSMO interface, they can attract charge with the opposite sign in the LSMO layer to the other side of the interface, as shown in Fig. 2(c). Since the STO substrate is insulating and there is no external source of charge compensation. Conservation of charge induces charge redistribution in the LSMO layer. In the P_{up} samples, negative charge (electron doping) migrates to the BFO/LSMO interface and positive charge (hole doping) remains at the LSMO/STO interface, resulting in formation of a transient charge gradient. The sign of charge redistribution is opposite for the P_{down} samples. The depth profile of LSMO magnetization should follow the charge gradient. To simulate such thickness dependence of electron/hole doping, here we use simplified magnetic depth profiles [Figs. 5(a)–5(c)] and theoretically calculated the corresponding angle/energy dependence of XMCDR [Figs. 5(d) and 5(e)] to mimic the transient behaviors of XMCDR. It could be clearly observed that although the total magnetization of the $\text{LSMO}_{0.2}$ layer remains the same for the simulated “ P_{up} ”, “ P_{down} ”, and “no polarization” cases, larger magnetization near the BFO/LSMO interface leads to a significantly larger XMCDR signal. This is because the finite penetration depth of the Mn L edge soft x ray makes the magnetic moments at deeper position contribute less to the XMCDR signal. The accumulation regime well agrees with the observed magnetic dynamic behaviors in Fig. 3. It should be noted that carrier injection from the STO substrate was interpreted as the mechanism of light-induced magnetism change of BFO/LSMO heterostructures in a pre-

vious report [21]. In our case, the carrier injection from the substrate should not depend on the BFO polarization, thus does not influence the validity of our interpretation.

In addition, we can estimate the size of the internal electric field which induces the FEPV effect. The modification of magnetic dynamics by the direction of BFO polarization mainly appears at a timescale of around 100 ps, and the average distance that the photocarriers travel from the place where they are generated to the BFO/LSMO interface can be assumed as ~ 20 nm (half of the BFO thickness). Simple calculation will result in a photocarrier drift speed of ~ 200 m/s. By using the formula $v = \mu E$, where v is the carrier drift speed and μ is the carrier mobility (~ 0.7 cm^2/Vs for BFO [6]), the size of the internal electric field could be estimated as $E \sim 3$ MV/m. Compared with the usually reported coercive field of several tens of MV/m in BFO, this value is reasonable when taking surface/interface charge screening into consideration.

IV. CONCLUSIONS

In summary, we have observed dynamics of photocarriers by monitoring the magnetic dynamics of adjacent FM layers. Different out-of-plane FE polarization can drive the photocarriers with different signs to accumulate at the FE/FM interface. To compensate the transient charge accumulation in the FE layer, the free carriers with the opposite charge sign in the FM layer migrate to the FE/FM interface, inducing a transient charge/magnetization redistribution in the FM layer. The timescale of these processes is around 100 ps. The FEPV-effect-induced magnetization change superposes with the photo-induced demagnetization, resulting in the magnetic dynamic behaviors of the FE/FM heterostructures. Our results clarify the photo-induced carrier transport behaviors at the FE/FM interface, which should be useful for development of novel light-manipulated magnetic devices and related applications.

ACKNOWLEDGMENTS

This work was supported by Natural Science Foundation of China (Grants No. 52002370 and No. 52102130), JSPS KAKENHI Grant No. 17F17327 and Basic Research Funding of IHEP (Grant No. Y9515560U1). We thank HZB for the allocation of synchrotron radiation beamtime (Proposals No. 202-09723ST/R, No. 201-09271ST, No. 191-07992ST, and No. 192-08474ST/R). We acknowledge the helpful discussion with K. Takubo and K. Yamamoto from University of Tokyo, as well as experimental supports provided by Karsten Hollandack and Rolf Mitzner from BESSY II, Professor J. X. Zhang from Beijing Normal University, Professor J. Ma, and Dr. M. F. Chen from Tsinghua University.

- [1] X. Han, Y. Ji, and Y. Yang, Ferroelectric photovoltaic materials and devices, *Adv. Funct. Mater.* **32**, 2109625 (2022).
 [2] C. Paillard, X. Bai, I. C. Infante, M. Guennou, G. Geneste, M. Alexe, J. Kreisel, and B. Dkhil, Photovoltaics with

- ferroelectrics: Current status and beyond, *Adv. Mater.* **28**, 5153 (2016).
 [3] V. M. Fridkin and B. Popov, Anomalous photovoltaic effect in ferroelectrics, *Sov. Phys. Usp.* **21**, 981 (1978).

- [4] L. W. Martin and A. M. Rappe, Thin-film ferroelectric materials and their applications, *Nat. Rev. Mater.* **2**, 16087 (2016).
- [5] S. Yang, J. Seidel, S. Byrnes, P. Shafer, C.-H. Yang, M. Rossell, P. Yu, Y.-H. Chu, J. Scott, J. Ager *et al.*, Above-bandgap voltages from ferroelectric photovoltaic devices, *Nat. Nanotechnol.* **5**, 143 (2010).
- [6] J. Seidel, D. Fu, S.-Y. Yang, E. Alarcón-Lladó, J. Wu, R. Ramesh, and J. W. Ager III, Efficient Photovoltaic Current Generation at Ferroelectric Domain Walls, *Phys. Rev. Lett.* **107**, 126805 (2011).
- [7] T. Choi, S. Lee, Y. Choi, V. Kiryukhin, and S.-W. Cheong, Switchable ferroelectric diode and photovoltaic effect in BiFeO₃, *Science* **324**, 63 (2009).
- [8] S. Yang, L. Martin, S. Byrnes, T. Conry, S. Basu, D. Paran, L. Reichertz, J. Ihlefeld, C. Adamo, A. Melville *et al.*, Photovoltaic effects in BiFeO₃, *Appl. Phys. Lett.* **95**, 062909 (2009).
- [9] Y. Zhou, C. Wang, S. Tian, X. Yao, C. Ge, E.-J. Guo, M. He, G. Yang, and K. Jin, Switchable ferroelectric diode and photovoltaic effects in polycrystalline BiFeO₃ thin films grown on transparent substrates, *Thin Solid Films* **698**, 137851 (2020).
- [10] W. Ji, K. Yao, and Y. C. Liang, Bulk photovoltaic effect at visible wavelength in epitaxial ferroelectric BiFeO₃ thin films, *Adv. Mater.* **22**, 1763 (2010).
- [11] J.-M. Hu, L.-Q. Chen, and C.-W. Nan, Multiferroic heterostructures integrating ferroelectric and magnetic materials, *Adv. Mater.* **28**, 15 (2016).
- [12] C. A. Vaz, Electric field control of magnetism in multiferroic heterostructures, *J. Phys.: Condens. Matter* **24**, 333201 (2012).
- [13] B. Chen, N. Gauquelin, N. Strkalj, S. Huang, U. Halisdemir, M. D. Nguyen, D. Jannis, M. F. Sarott, F. Eltes, S. Abel *et al.*, Signatures of enhanced out-of-plane polarization in asymmetric BaTiO₃ superlattices integrated on silicon, *Nat. Commun.* **13**, 265 (2022).
- [14] R. Wu, D. Zhang, T. Maity, P. Lu, J. Yang, X. Gao, S. Zhao, X. Wei, H. Zeng, A. Kursumovic *et al.*, Self-biased magnetoelectric switching at room temperature in three-phase ferroelectric-antiferromagnetic-ferrimagnetic nanocomposites, *Nat. Electron.* **4**, 333 (2021).
- [15] C.-L. Jia, T.-L. Wei, C.-J. Jiang, D.-S. Xue, A. Sukhov, and J. Berakdar, Mechanism of interfacial magnetoelectric coupling in composite multiferroics, *Phys. Rev. B* **90**, 054423 (2014).
- [16] X. Yao, J. Ma, Y. Lin, C. Nan, and J. Zhang, Magnetoelectric coupling across the interface of multiferroic nanocomposites, *Sci. China Mater.* **58**, 143 (2015).
- [17] J. Scott, Multiferroic memories, *Nat. Mater.* **6**, 256 (2007).
- [18] A. Roy, R. Gupta, and A. Garg, Multiferroic memories, *Adv. Condens. Matter Phys.* **2012**, 926290 (2012).
- [19] M. M. Vopson, Fundamentals of multiferroic materials and their possible applications, *Crit. Rev. Solid State Mater. Sci.* **40**, 223 (2015).
- [20] R. Zhao, J. Wang, J. Ma, J. Ma, and C.-W. Nan, Polarization control of photoconductivity in BiFeO₃/La_{1-x}Sr_xMnO₃ ($x = 0.33, 0.5$) heterostructures, *Ceram. Intl.* **45**, 19550 (2019).
- [21] K. Sung, T. Lee, Y. Park, N. Hur, and J. Jung, Photo-carrier control of exchange bias in BiFeO₃/La_{2/3}Sr_{1/3}MnO₃ thin films, *Appl. Phys. Lett.* **104**, 252407 (2014).
- [22] M. Zheng, H. Ni, X. Xu, Y. Qi, X. Li, and J. Gao, Optically Tunable Resistive-Switching Memory in Multiferroic Heterostructures, *Phys. Rev. Appl.* **9**, 044039 (2018).
- [23] L. You, F. Zheng, L. Fang, Y. Zhou, L. Z. Tan, Z. Zhang, G. Ma, D. Schmidt, A. Rusydi, L. Wang *et al.*, Enhancing ferroelectric photovoltaic effect by polar order engineering, *Sci. Adv.* **4**, eaat3438 (2018).
- [24] H. Wen, P. Chen, M. P. Cosgriff, D. A. Walko, J. H. Lee, C. Adamo, R. D. Schaller, J. F. Ihlefeld, E. M. Dufresne, D. G. Schlom *et al.*, Electronic Origin of Ultrafast Photoinduced Strain in BiFeO₃, *Phys. Rev. Lett.* **110**, 037601 (2013).
- [25] M. Lejman, G. Vaudel, I. C. Infante, P. Gemeiner, V. E. Gusev, B. Dkhil, and P. Ruello, Giant ultrafast photo-induced shear strain in ferroelectric BiFeO₃, *Nat. Commun.* **5**, 4301 (2014).
- [26] H. J. Lee, Y. Ahn, S. D. Marks, D. Sri Gyan, E. C. Landahl, J. Y. Lee, T. Y. Kim, S. Unithrattil, S. H. Chun, S. Kim *et al.*, Subpicosecond optical stress generation in multiferroic BiFeO₃, *Nano Lett.* **22**, 4294 (2022).
- [27] D. Daranciang, M. J. Highland, H. Wen, S. M. Young, N. C. Brandt, H. Y. Hwang, M. Vattilana, M. Nicoul, F. Quirin, J. Goodfellow *et al.*, Ultrafast Photovoltaic Response in Ferroelectric Nanolayers, *Phys. Rev. Lett.* **108**, 087601 (2012).
- [28] H.-C. Mertins, D. Abramsohn, A. Gaupp, F. Schäfers, W. Gudat, O. Zaharko, H. Grimmer, and P. M. Oppeneer, Resonant magnetic reflection coefficients at the Fe 2*p* edge obtained with linearly and circularly polarized soft x rays, *Phys. Rev. B* **66**, 184404 (2002).
- [29] T. Tsuyama, S. Chakraverty, S. Macke, N. Pontius, C. Schübler-Langeheine, H. Y. Hwang, Y. Tokura, and H. Wadati, Photoinduced Demagnetization and Insulator-to-Metal Transition in Ferromagnetic Insulating BaFeO₃ Thin Films, *Phys. Rev. Lett.* **116**, 256402 (2016).
- [30] H. Fujishiro, T. Fukase, and M. Ikebe, Charge ordering and sound velocity anomaly in La_{1-x}Sr_xMnO₃ ($x \geq 0.5$), *J. Phys. Soc. Jpn.* **67**, 2582 (1998).
- [31] J. Hemberger, A. Krimmel, T. Kurz, H.-A. K. Von Nidda, V. Y. Ivanov, A. A. Mukhin, A. M. Balbashov, and A. Loidl, Structural, magnetic, and electrical properties of single-crystalline La_{1-x}Sr_xMnO₃ ($0.4 < x < 0.85$), *Phys. Rev. B* **66**, 094410 (2002).
- [32] Y. Tian, L. Wei, Q. Zhang, H. Huang, Y. Zhang, H. Zhou, F. Ma, L. Gu, S. Meng, L.-Q. Chen *et al.*, Water printing of ferroelectric polarization, *Nat. Commun.* **9**, 3809 (2018).
- [33] D. Sando, C. Carrétéro, M. N. Grisolia, A. Barthélémy, V. Nagarajan, and M. Bibes, Revisiting the optical band gap in epitaxial BiFeO₃ thin films, *Adv. Opt. Mater.* **6**, 1700836 (2018).
- [34] X. S. Xu, T. V. Brinzari, S. Lee, Y. H. Chu, L. W. Martin, A. Kumar, S. McGill, R. C. Rai, R. Ramesh, V. Gopalan, S. W. Cheong, and J. L. Musfeldt, Optical properties and magneto-chromism in multiferroic BiFeO₃, *Phys. Rev. B* **79**, 134425 (2009).
- [35] V. Železný, D. Chvostová, L. Pajasová, I. Vrejoiu, and M. Alexe, Optical properties of epitaxial BiFeO₃ thin films, *Appl. Phys. A* **100**, 1217 (2010).
- [36] H. L. Liu, M. Lin, Y. Cai, C. Tung, and Y. Chu, Strain modulated optical properties in BiFeO₃ thin films, *Appl. Phys. Lett.* **103**, 181907 (2013).
- [37] Y. Du, M.-S. Zhang, J. Wu, L. Kang, S. Yang, P. Wu, and Z. Yin, Optical properties of SrTiO₃ thin films by pulsed laser deposition, *Appl. Phys. A* **76**, 1105 (2003).
- [38] R. Thomas and D. Dube, Optical properties of sol-gel processed amorphous and crystalline SrTiO₃ thin films, *Jpn. J. Appl. Phys.* **39**, 1771 (2000).

- [39] Y. Gao, Y. Masuda, and K. Koumoto, Band gap energy of SrTiO₃ thin film prepared by the liquid phase deposition method, *J. Korean Ceram. Soc.* **40**, 213 (2003).
- [40] CXRO x-ray database, online https://henke.lbl.gov/optical_constants/, accessed: 2023-01-03.
- [41] S. Macke and E. Goering, Magnetic reflectometry of heterostructures, *J. Phys.: Condens. Matter* **26**, 363201 (2014).
- [42] B. L. Henke, E. M. Gullikson, and J. C. Davis, X-ray interactions: photoabsorption, scattering, transmission, and reflection at E= 50-30,000 eV, Z= 1-92, *At. Data Nucl. Data Tables* **54**, 181 (1993).
- [43] C. Aruta, G. Ghiringhelli, V. Bisogni, L. Braicovich, N. B. Brookes, A. Tebano, and G. Balestrino, Orbital occupation, atomic moments, and magnetic ordering at interfaces of magnetite thin films, *Phys. Rev. B* **80**, 014431 (2009).
- [44] G. M. Müller, J. Walowski, M. Djordjevic, G.-X. Miao, A. Gupta, A. V. Ramos, K. Gehrke, V. Moshnyaga, K. Samwer, J. Schmalhorst *et al.*, Spin polarization in half-metals probed by femtosecond spin excitation, *Nat. Mater.* **8**, 56 (2009).
- [45] See Supplemental Material at <http://link.aps.org/supplemental/10.1103/PhysRevB.107.L220303> for x-ray diffraction patterns of the BFO/LSMO heterostructures; static soft x-ray reflectivity and XMCDR and magnetic hysteresis loop measured in resonant reflectivity for the BFO/LSMO heterostructures; estimation of heat diffusion time and transient thermal expansion of BFO, which also contains Refs. [46–49].
- [46] L. Chen, J. Yang, C.-W. Luo, C. Laing, K.-H. Wu, J.-Y. Lin, T. Uen, J.-Y. Juang, Y. Chu, and T. Kobayashi, Ultrafast photoinduced mechanical strain in epitaxial BiFeO₃ thin films, *Appl. Phys. Lett.* **101**, 041902 (2012).
- [47] P. Ruello, T. Pezeril, S. Avanesyan, G. Vaudel, V. Gusev, I. C. Infante, and B. Dkhil, Photoexcitation of gigahertz longitudinal and shear acoustic waves in BiFeO₃ multiferroic single crystal, *Appl. Phys. Lett.* **100**, 212906 (2012).
- [48] J. Bucci, B. Robertson, and W. James, The precision determination of the lattice parameters and the coefficients of thermal expansion of BiFeO₃, *J. Appl. Cryst.* **5**, 187 (1972).
- [49] V. Juve, R. Gu, S. Gable, T. Maroutian, G. Vaudel, S. Matzen, N. Chigarev, S. Raetz, V. E. Gusev, M. Viret, A. Jarnac, C. Laulhe, A.A. Maznev, B. Dkhil, and P. Ruello, Ultrafast light-induced shear strain probed by time-resolved x-ray diffraction: Multiferroic BiFeO₃ as a case study, *Phys. Rev. B* **102**, 220303(R) (2020).